JGR Solid Earth

RESEARCH ARTICLE
10.1029/2021JB022161

Continuous Tremor Activity With Stable Polarization Direction Following the 2014 Large Slow Slip Event in the Hikurangi Subduction Margin Offshore New Zealand

Yuriko Iwasaki[1,2], Kimihiro Mochizuki[1], Motoko Ishise[1], Erin K. Todd[3], Susan Y. Schwartz[4], Hubert Zal[5], Martha K. Savage[5], Stuart Henrys[6], Anne F. Sheehan[7], Yoshihiro Ito[8], Laura M. Wallace[6,9], Spahr C. Webb[10], Tomoaki Yamada[1], and Masanao Shinohara[1]

[1]Earthquake Research Institute, University of Tokyo, Tokyo, Japan, [2]Now at: Japan Meteorological Agency, Tokyo, Japan, [3]Golder Associates (NZ) Ltd., Christchurch, New Zealand, [4]Department of Earth and Planetary Sciences, University of California Santa Cruz, Santa Cruz, CA, USA, [5]Victoria University of Wellington, Wellington, New Zealand, [6]GNS Science, Lower Hutt, New Zealand, [7]Department of Geological Sciences, Cooperative Institute for Research in Environmental Sciences, University of Colorado Boulder, Boulder, CO, USA, [8]Disaster Prevention Research Institute, Kyoto University, Kyoto, Japan, [9]University of Texas Institute for Geophysics (UTIG), Austin, TX, USA, [10]Lamont-Doherty Earth Observatory (LDEO), Columbia University, Palisades, NY, USA

Abstract Many types of slow earthquakes have been discovered at subduction zones around the world. However, the physical process of these slow earthquakes is not well understood. To monitor offshore slow earthquakes, a marine seismic and geodetic experiment was conducted at the Hikurangi subduction margin from May 2014 to June 2015. During this experiment, a large slow slip event (Mw 6.8) occurred directly beneath the ocean bottom seismometer (OBS) network. In this study, S-wave splitting and polarization analysis methods, which have been previously used on onshore data to investigate tremor and anisotropy, are applied to continuous OBS waveform data to identify tremors that are too small to detect by the envelope cross correlation method. Continuous tremor activity with stable polarization directions is detected at the end of the 2014 slow slip event and continued for about 2 weeks. The tremors are generated around a southwest bend in the slow slip contours and at the landward edge of a subducted seamount. Our findings corroborate a previous interpretation, based on burst-type repeating earthquakes and intermittent tremor, that localized slow slip and tremor around the seamount was triggered by fluid migration following the large plate boundary slow slip event and indicate tremor occurred continuously rather than as isolated and sporadic individual events.

Plain Language Summary Slow earthquakes and tremor are characterized by slow fault rupture. Their generation mechanism has not been well understood. The slow earthquake itself does not cause damage but may inform forecasts of large earthquakes that could cause strong ground shaking or tsunamis. A large slow slip event occurred on the Hikurangi subduction plate boundary, offshore New Zealand, in 2014 directly beneath a temporary ocean bottom seismometer network. We applied new methods to this data to detect and characterize an earthquake tremor signal. The methods determine the polarization of the wave emanating from the tremor and the fast direction of the anisotropic subsurface structure through which the tremor wave propagates. These parameters enable us to detect small amplitude tremors and to determine their spatial and temporal distribution. We observed continuous tremor activity for about 2 weeks duration while the slow slip event was waning. This tremor activity occurred over a mapped subducted seamount and on the plate boundary, which likely experienced large stress changes due to the slow slip event. Our results are consistent with previous studies that used different methods on the same data, which indicate that the tremor activity in the vicinity of the seamount was triggered by fluid migration.

Key Points:

- S-wave splitting and polarization analyses of continuous offshore data detect small amplitude tremor activity
- Tremor activity with stable polarization direction started near the end of the 2014 Gisborne slow slip event (SSE) and was continuous for about 2 weeks
- Tremor activity occurred around the landward edge of the subducted seamount and was triggered by fluid migration following the SSE

Supporting Information:

Supporting Information may be found in the online version of this article.

Correspondence to:

Y. Iwasaki,
y-iwasaki@met.kishou.go.jp

Citation:

Iwasaki, Y., Mochizuki, K., Ishise, M., Todd, E. K., Schwartz, S. Y., Zal, H., et al. (2022). Continuous tremor activity with stable polarization direction following the 2014 large slow slip event in the Hikurangi subduction margin offshore New Zealand. *Journal of Geophysical Research: Solid Earth*, *127*, e2021JB022161. https://doi.org/10.1029/2021JB022161

Received 27 APR 2021
Accepted 8 NOV 2021

1. Introduction

Slow earthquakes are phenomena characterized by slow fault rupture. Many types of slow earthquakes at subduction zones around the world have been reported (e.g., Obara & Kato, 2016). However, the physical processes of these slow earthquakes are not yet thoroughly understood. Models that explain the mechanisms of various types of slow earthquakes have been proposed. Ito et al. (2007) suggested one possible model, in which patches failing in very low frequency (VLF) earthquakes are surrounded by aseismic slow slip regions bearing micro cracks with

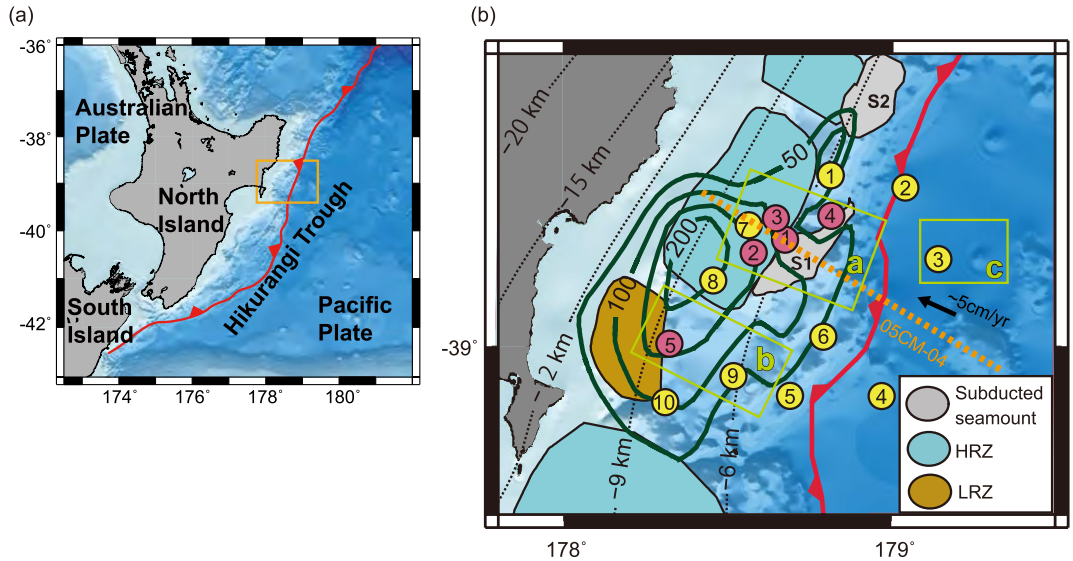

Figure 1. (a) Tectonic setting of the Hikurangi subduction margin, offshore New Zealand. (b) The region outlined by orange rectangle in Figure 1a. Depth of the plate interface (Williams et al., 2013) is shown with black broken lines. Very dark green contour lines show slip distribution (in millimeters) of the late September–early October 2014 Gisborne SSE (Wallace et al., 2016). The EOBSs and LOBSs in the Hikurangi Ocean Bottom Investigation of Tremor and Slow slip experiment are shown by red circles and yellow circles, respectively. Subducted seamounts (S1 and S2), high-amplitude reflectivity zones (HRZ), and lens reflectivity zone (LRZ) are from Bell et al. (2010). The updated outline of seamount S1 is from Barker et al. (2018). HRZs are zones that are interpreted to be rich in fluid near the plate interface. The location of seismic profile 05CM-04 (Figure 11) is shown with orange dotted lines. The regions outlined by bright green rectangles contain the OBS groups shown in Figures 6a–6c The black arrow indicates the convergence direction between the Pacific Plate and the North Island at the Hikurangi Trough (Wallace et al., 2004).

source sizes smaller than those of VLF earthquakes. Those micro cracks may generate low frequency tremor. Ide (2008) proposed a Brownian walk model that explains various features of slow earthquakes from tremor to slow slip event (SSE). The relationship between SSE and tremor is also still being studied. Because of well-established spatial and temporal correlations between tremor and slow slip, known as episodic tremor and slip (e.g., Rogers & Dragert, 2003), tremors are used as a tool for monitoring slow slip (e.g., Hiramatsu et al., 2008). However, Wech and Bartlow (2014) observed that slow slip on a tremor-generating fault can change from tremorgenic to silent and back again. They found that the tremor turned silent when the rupture speed during a SSE was reduced. Therefore, they suggest use of tremor as a slip meter may be limited. Our goal here is to reveal the spatiotemporal distribution of slow earthquakes in order to gain a better understanding of its physical processes.

The Hikurangi subduction margin is one of the subduction zones where slow earthquakes have been best observed (Figure 1). Repeating SSEs have been well-recorded by New Zealand GeoNet's GNSS network along the entire Hikurangi subduction margin (e.g., Wallace & Beavan, 2010; Wallace et al., 2012). At the northern end of this margin, shallow SSEs with equivalent seismic moments between Mw 6.3–6.8 occur every 18–24 months and last 1–5 weeks (e.g., Wallace & Beavan, 2010). Such frequent occurrence of slow earthquakes makes the Hikurangi subduction margin an ideal place to investigate slow earthquakes with field studies. Low-frequency tremors beneath the land accompanying northern Hikurangi SSEs were detected and located by Kim et al. (2011) and Todd and Schwartz (2016). Yet offshore low frequency tremor spatially collocated with SSEs had not been detected prior to the 2014 Gisborne SSE. In 2014, a Mw 6.8 SSE occurred offshore Gisborne, New Zealand. This SSE occurred directly beneath the ocean bottom seismometer (OBS) and absolute pressure gauge (APG) network deployed during the Hikurangi Ocean Bottom Investigation of Tremor and Slow slip (HOBITSS) experiment (Wallace et al., 2016). Offshore shallow tremors, spatially collocated with the 2014 Gisborne slow slip, were for the first time detected and located using the envelope cross correlation method by Todd et al. (2018). However, the number of located tremors was smaller than that expected from tremor apparent in the waveforms and spectrograms. For example, we will show in Section 4.1 that we can observe tremor-like waveforms continuously, but during the time, no tremor was located by the envelope cross correlation method. This may be due to characteristics of the Hikurangi subduction margin such as its shallow plate interface (Figure 1), and high

seismic attenuation in the overriding plate (Nakai et al., 2021), which makes it difficult to correlate tremor across multiple stations. Several other seismic measurements suggested that the properties near the SSE changed during the SSE. Warren-Smith et al. (2019) used stress inversions from earthquake focal mechanisms to show that the ratio between the relative magnitudes of stress components for earthquakes below the plate interface decreased before this and other SSEs and then rose again during the SSEs. Zal et al. (2020) determined average S-wave splitting (SWS) parameters from local earthquakes (sensitive to the top several km of the upper plate) recorded during the deployment to show that delay times increased and the ratio of compressional to shear wave velocity (V_p/V_s) decreased prior to the SSE, while the delay times decreased and V_p/V_s increased during the SSE. An interpretation consistent with both data sets is that plate convergence caused cracks in the upper plate to close so that pressurized fluid built up under a seal on the plate interface before the SSE. The SSE then broke the seal, lowering the fluid pressure in the subducting plate and allowing fluid to flow through the upper plate, making the cracks rounder and allowing them to retain more pore water.

In this study, we applied polarization and SWS analyses on continuous waveforms to identify tremor. This method is applicable even when only a few OBSs are available. Previous studies (e.g., Bostock & Christensen, 2012; Imanishi et al., 2016) using these analyses focused on investigating anisotropy or focal mechanisms of tremor by using waveforms of tremors whose hypocenters had already been determined. These studies found that the parameters obtained by polarization and SWS analyses become stable while tremor activity is ongoing in the vicinity and are random when tremor activity is not occurring. Based on these results, Ishise and Nishida (2016) suggested that tremor can be detected by inspecting polarization and SWS parameters from land data. In this study, we apply polarization and SWS analyses to OBS data to detect small shallow tremors that have not previously been detected.

The shallow plate interface at the Hikurangi subduction margin has been investigated in detail by seismic reflection surveys. The resulting images reveal heterogeneous structures on the plate interface such as subducted seamounts (Barker et al., 2018; Bell et al., 2010). Subducted seamounts are thought to play an important role in interseismic coupling along subduction zone megathrusts. Some studies (e.g., Scholz & Small, 1997) suggest seamount subduction will enhance local seismic coupling and can be the nucleation source of large earthquakes. Other studies (e.g., Mochizuki et al., 2008; Wang & Bilek, 2011) suggest that the plate interface at subducted seamounts is not well coupled due to formation of a fracture network where the seamount is subducted. The slip distribution of the 2014 Gisborne SSE, obtained by Wallace et al. (2016), suggests that slow slip along the plate interface decreased in the region of the subducted seamount (Figure 1). In this study, we present the spatiotemporal behavior of tremor and discuss its relationship to slow slip and the subducted seamount.

2. Data and Methodology

We used data obtained by the HOBITSS experiment. This experiment was conducted from May 2014 to June 2015 (Todd, 2014). 24 APGs and 15 OBSs were deployed. The OBS network consisted of 5 Earthquake Research Institute type OBSs (EOBSs) and 10 Lamont Doherty Earth Observatory type OBSs (LOBSs); the locations of the OBSs are shown in Figure 1. EOBS and LOBS were equipped with 3-component velocity sensors with a natural period of 1 and 120 s, respectively. Unfortunately, LOBS 4 and 5 recorded no usable data during the SSE. LOBS 3, 7, 9, and 10 had a problem with the clock timing of their recorders. The nature of the timing errors is still under investigation, but they range between a few seconds to tens of seconds. These small timing differences between stations will not affect the polarization and SWS analyses. At LOBS 1, 2, 6, 8, and 10, we found that our analysis did not reliably differentiate tremor from noise. Therefore, in this study, we used all 5 EOBSs and LOBS 3, 7, and 9. The OBSs were deployed from a ship and placed on the seafloor by free fall. Therefore, we did not have control of the orientation of the horizontal components at the seafloor. The orientations were determined using P and Rayleigh waves by Zal et al. (2020) after recovery. During the HOBITSS experiment, a Mw 6.8 SSE that lasted 2–3 weeks occurred in late September 2014 directly beneath the array (Wallace et al., 2016).

We applied the polarization and SWS analysis methods of Bostock and Christensen (2012) and Ishise and Nishida (2016) to the OBS waveforms. These studies used waveform data obtained from onshore seismic networks in northern Cascadia and Shikoku, respectively. A schematic illustration of the relationship between the parameters obtained from polarization and SWS analyses is shown in Figure 2. Tremor energy is considered to consist primarily of S-waves as mentioned in Bostock and Christensen (2012). Seismic energy of tremor is

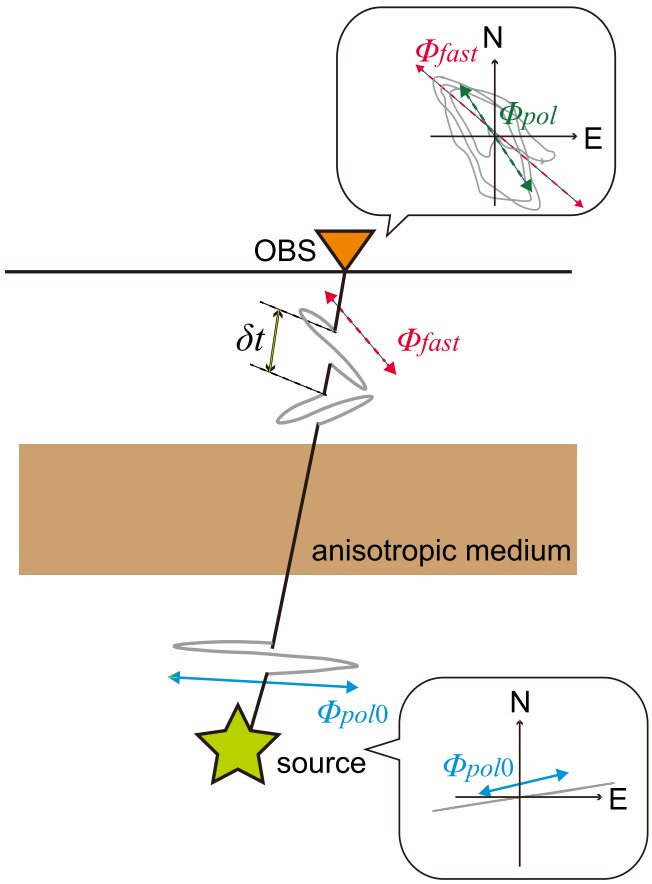

Figure 2. Schematic drawing of the relationship between ϕ_{pol0}, ϕ_{fast}, δt and ϕ_{pol}. Initially, the S-wave from the source is polarized in a certain direction that reflects the focal mechanism at the source. At the start the particle motion of the wave is linear. Then the wave propagates through the anisotropic medium and splits. As a result, the polarization of the wave observed at the ocean bottom seismometer station includes the effect of the splitting and the particle motion is elliptical.

expected to arrive at the OBSs with nearly vertical ray paths, due to a low velocity sediment layer under the OBSs, resulting in nearly horizontal polarizations. Therefore, we conducted principal component analysis using waveforms of the horizontal components. Specifically, we compute the covariance matrix of the horizontal component velocity data and derive its eigenvectors $\boldsymbol{s}_i$ and associated eigenvalues λ_i, $i = 1, 2$, sorted in descending order. This analysis yields the polarization direction (ϕ_{pol}) and degree of polarization (λ_2/λ_1) in the horizontal plane. For the SWS analysis, seismograms of horizontal components are rotated from 0 to 180° by 1° increments and shifted in time by −0.5 to 0.5 s (lag) with increments of 0.005 s for EOBS and of 0.01 s for LOBS. The difference in the increments in time is derived from a difference in sampling rate. Cross-correlation coefficients (CC) between components are calculated at each rotation angle and time lag. The rotation angle and time lag that maximizes the CC is found. In our calculations, if the time lag is a positive value, the rotation angle and the time lag represent the fast direction (ϕ_{fast}) and delay time (δt), respectively. On the other hand, if the time lag is a negative value, ϕ_{fast} is normal to the rotation angle and the delay time is the absolute value of the time lag, and we report it as a positive value. This method is almost the same as that of Bowman and Ando (1987). In this paper, we distinguish time lag and δt. We extract 30 s long time series from the year-long velocity data every 10 s and apply the polarization and SWS analyses. As in previous studies (e.g., Imanishi et al., 2016), in order to increase the signal-to-noise ratio but not mix seismic waves from disparate source locations, we use a 30 s time window. Due to slow rupture propagation, the source location of tremor should not vary much within the 30 s time window and ϕ_{pol} and SWS parameters should remain relatively stable. At the stations where we observed clear SWS, we also recover an estimate of the original polarization direction (ϕ_{pol0}). To calculate ϕ_{pol0} for every 30 s time window we rotate the horizontal components to the calculated fast and slow directions and time shift them by δt.

The data are noisy at frequencies below about 2 Hz (microseisms) and in the frequency band between 5 and 10 Hz at some OBSs (Figure S1 in Supporting Information S1). Therefore, we applied a 2–5 Hz band-pass filter to remove noise for all OBS data (about 200–500 m wavelength at the top of the crust). In general, the signal-to-noise ratio is smaller on OBS data than on onshore data. Thus, we applied a new additional preconditioning procedure to the OBS data. To distinguish seismic signals from noise, we considered the distribution of the CCs obtained from SWS analysis of the year-long data. Since CCs of the signal should be high, we set a CC threshold for each station and retained the results from the SWS and polarization analyses only at times when the CCs were above the chosen threshold. To extract these signals, we calculate the distribution of CCs in the entire data set (May 2014 to June 2015) with the exception of September, October, and November when the SSE and repeating earthquakes identified by Shaddox and Schwartz (2019) occur. For most of the stations, we set the threshold as the value below which 95% of the CCs occur. We observed noise with high CC frequently at LOBS 3 and 7 (yellow shaded rectangle in Figures 3, S2f, and S2g in Supporting Information S1) suggesting the 95% confidence interval excludes too much of the signal. Thus, for these stations, we use the 90% confidence interval as the threshold. The threshold at each station is indicated with the distribution of CC obtained from data in October and July in Figure S2 in Supporting Information S1.

3. Results

Parameters obtained from polarization analysis at EOBS 3 from October to early November are shown with the time interval of the SSE in Figures 4 and 5. ϕ_{pol} during the same period at other stations is shown in Figure 6. Based on the characteristics observed in Figure 6 we divided the OBSs into three groups, (a) near subducted

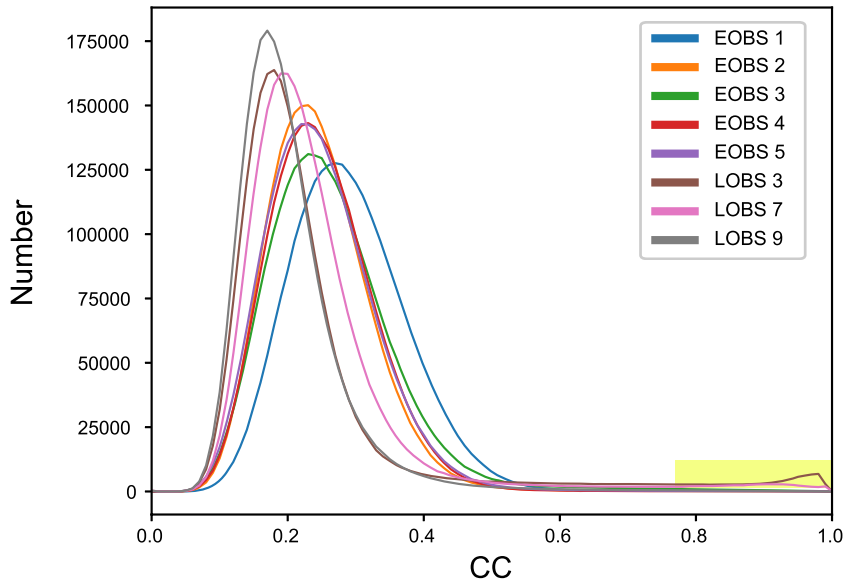

Figure 3. Distributions of Cross-correlation coefficients (CC) obtained from S-wave splitting analysis of all 5 EOBSs and LOBS 3, 7, and 9 by using year-long data (May 2014 to June 2015) with the exception of September, October, and November when SSE or repeating earthquakes occur. The area of abnormally high frequencies of high CC at LOBS 3 and 7 is highlighted with a yellow shaded rectangle.

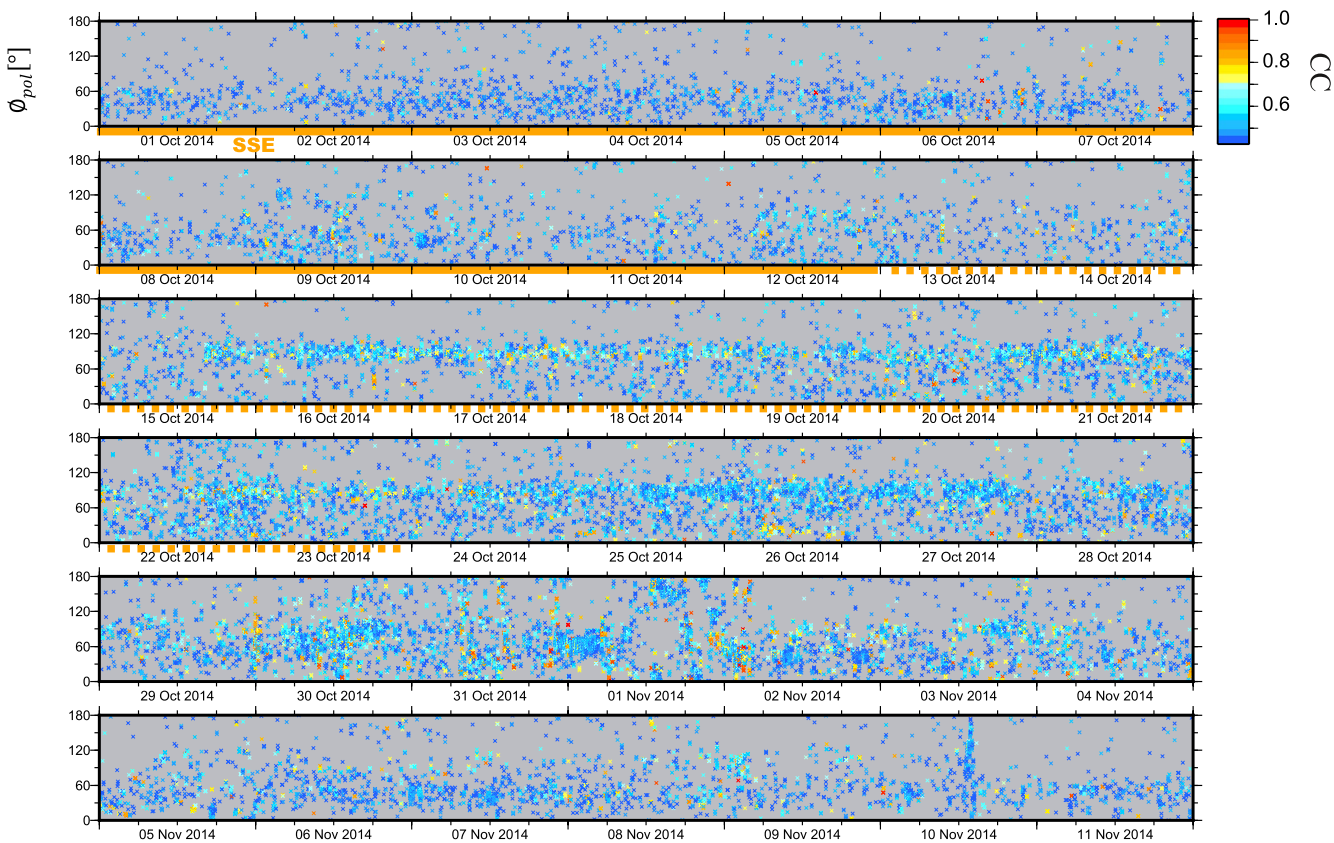

Figure 4. Time series from October 1 to November 11 of ϕ_{pol} [°] observed at EOBS 3 and colored according to the value of Cross-correlation coefficients. ϕ_{pol} is measured clockwise from north. The main pulse of the late September–early October 2014 Gisborne SSE (Wallace et al., 2016) is shown by the orange bar (from September 22 to October 12). The period when the slow slip event was tapering off (Yohler et al., 2019) is shown with the dashed orange bar (from October 13 to October 23).

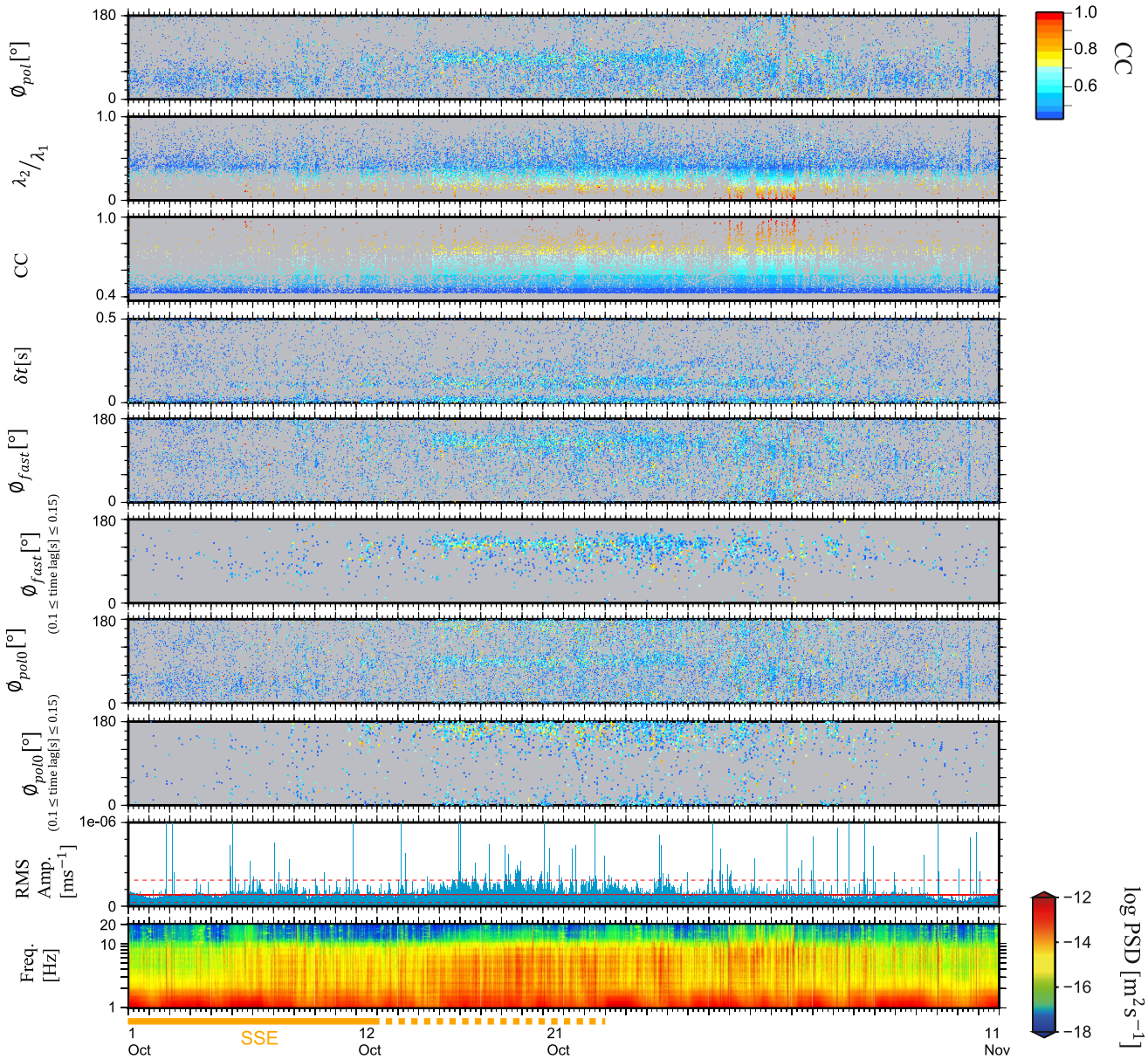

Figure 5. Times series from October 1 to November 11 of polarization and S-wave splitting parameters for EOBS 3. The panels show, in descending order, ϕ_{pol}, λ_2/λ_1, Cross-correlation coefficients (CC), δt, ϕ_{fast}, ϕ_{fast} ($0.1 \leq$ time lag[s] ≤ 0.15), ϕ_{pol0}, ϕ_{pol0} ($0.1 \leq$ time lag[s] ≤ 0.15), root mean square (RMS) amplitude and running spectrum. RMS amplitude was calculated from the 2–5 Hz filtered data of 2 horizontal components every 30 minutes. Colored and broken lines show the average value and the upper and lower bounds of a 95% confidence interval (within which 95% of the RMS amplitude occurs) calculated by using the data from June 2014 to May 2015 with the exception of September, October and November when slow slip event (SSE) or repeating earthquakes occur. The power spectral density is calculated using a window length of 12 minutes using one of the horizontal components. ϕ_{pol}, λ_2/λ_1, CC, δt, ϕ_{fast} and ϕ_{pol0} are colored according to the value of the of CC. ϕ_{pol}, ϕ_{fast} and ϕ_{pol0} are measured clockwise from north. The late September–early October 2014 Gisborne SSE (Wallace et al., 2016; Yohler et al., 2019) is shown by the orange bar and the dashed orange bar in the same manner as in Figure 4. The ϕ_{pol} is the same as that shown in Figure 4.

seamount S1, (b) near LOBS 9 and (c) LOBS 3; each group is indicated in Figure 1b. At EOBS 3, nearing the end of the reported SSE (October 15) and continuing for about 2 weeks, we observe continuous high CC signals exhibiting stable ϕ_{pol}. About a week before the start of this signal at EOBS 3, we observe continuous high CC signals exhibiting stable ϕ_{pol} with a similar duration at EOBS 2 and LOBS 9 (Figure 6). At roughly the same time LOBS 7 exhibits an intermittently stable ϕ_{pol} (near 150°) with about a 2-week duration (Figure 6a). At EOBS 1, ϕ_{pol} shows a scattered distribution with a stable orientation (near 150°) during most of the year-long experiment. However, at the beginning of the consistent polarization signal at EOBS 2 on October 8, ϕ_{pol} at EOBS 1 started

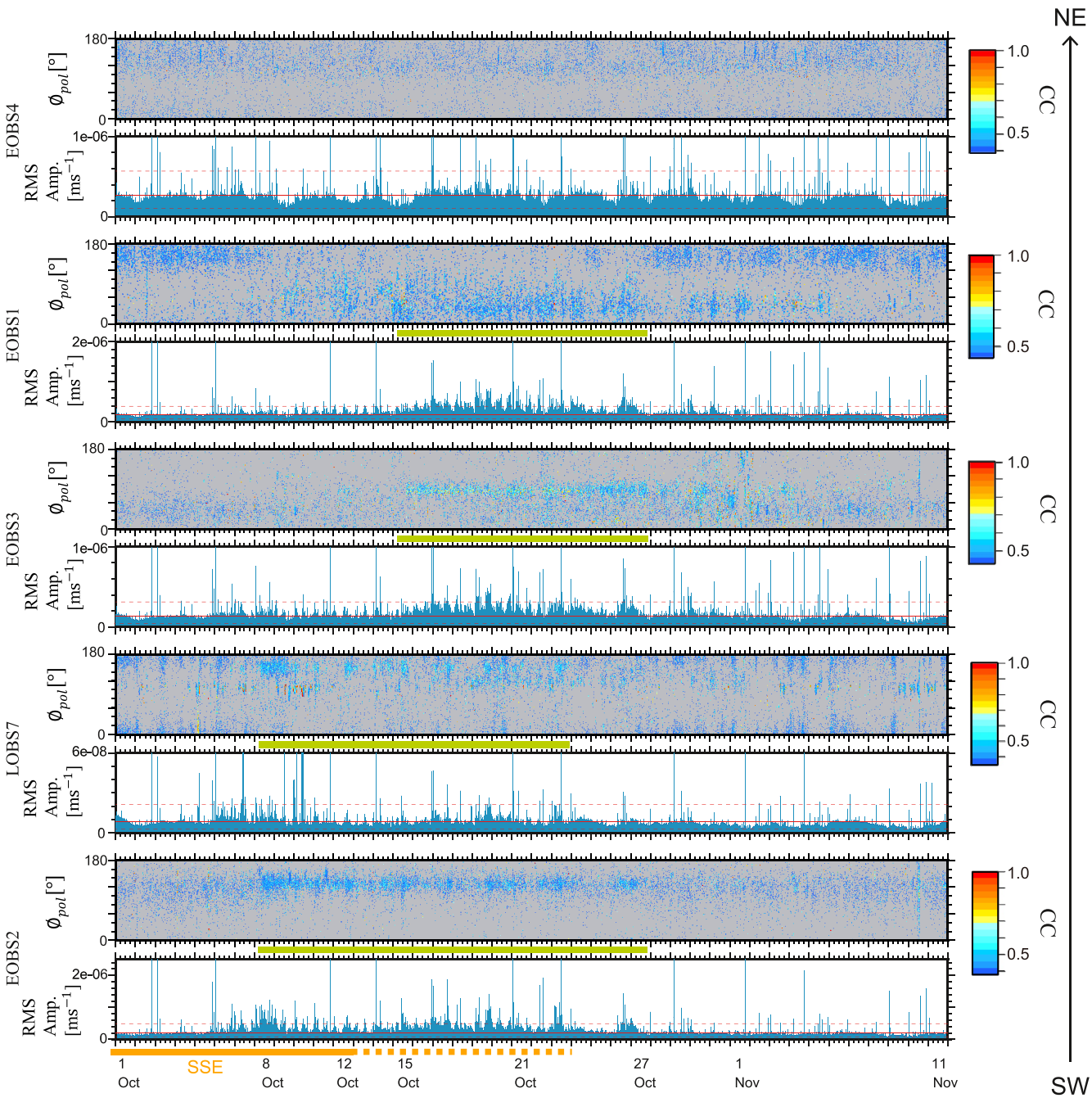

Figure 6. Times series from October 1 to November 11 of root mean square (RMS) amplitude [ms^{-1}] and ϕ_{pol} [°] for all OBSs used in this study. RMS amplitude was calculated from the 2–5 Hz filtered data of the two horizontal components every 30 minutes. Colored line and broken lines are indicated in the same manner as in Figure 5. OBSs are divided into three groups with respect to; (a) near subducted seamount S1, (b) near LOBS 9 and (c) LOBS 3 (see Figure 1b for locations). In (a), panels of OBSs are displayed in order from northeast to southwest, with respect to seamount S1. Green bars indicate the time of continuous signal at each station. The late September–early October 2014 Gisborne slow slip event (Wallace et al., 2016; Yohler et al., 2019) is shown by the orange bar and the dashed orange bar in the same manner as in Figure 4.

to change its polarization to a scattered distribution centered around 60°. Synchronous with the appearance of the continuous signal at EOBS 3, the distribution of ϕ_{pol} at EOBS1 appeared more concentrated at around 30° with high CC values that continue for about 2 weeks. During periods of stable ϕ_{pol}, λ_2/λ_1 is consistently low,

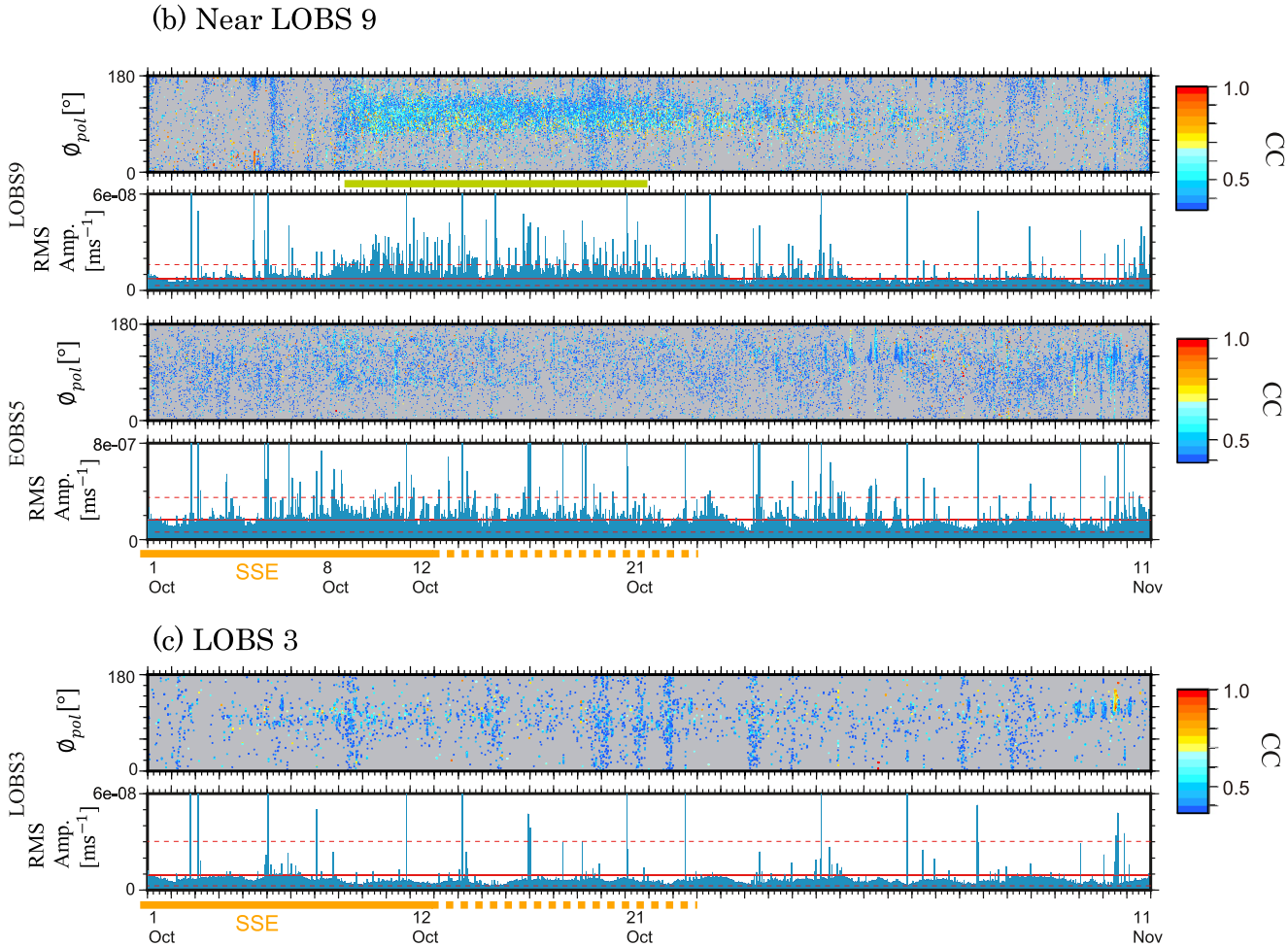

Figure 6. *Continued*

representing a strong polarization (Figure 5). We observed no similar behavior during the rest of the year-long experiment at EOBS 1, 2, and 3 and LOBS 7 and 9 (Figure S3 in Supporting Information S1). No continuous polarization signals were ever observed during the year-long experiment at EOBS 4 in group-a, EOBS 5 in group-b and, LOBS 3 in group-c. Daily average orientations of ϕ_{pol} during the continuous signals at EOBS 2 and LOBS 7 are calculated using day-long data and plotted at the respective OBS sites in Figure 7a.

Parameters obtained from SWS analysis are shown in Figures 5 and 8. At EOBS 3 (Figure 5), we observed stable ϕ_{fast} during the same time period as stable ϕ_{pol}. During that time, the CC was consistently high. However, we observed a bimodal distribution of δt near 0 and 0.1 s. It is possible that this is due to cycle skipping during waveform correlation calculations in which high CC values appear every half cycle around its maximum. Cycle skipping is a problem for SWS measurements and it occurs most frequently when the waveforms contain monotonic oscillations (e.g., Castellazzi et al., 2015). At LOBS 9 (Figure 8), we also observed scattered ϕ_{fast} within a certain range (from 60° to 150°) and a trimodal distribution of δt at roughly equal intervals (near 0, 0.1 and 0.2 s) at the same time as stable ϕ_{pol}. At EOBS 1, the delay time δt and fast direction ϕ_{fast} appear to exhibit stable values (near 0.3 s and near 120°, respectively) during the year-long observation. However, from the time when we observed unusual ϕ_{pol} at this station (from October 8), we also observed unstable ϕ_{fast} that appeared to exhibit a bimodal distribution at a 90° interval (around 60° and 150°). At the same time, δt showed a scattered distribution and a tendency of 4 peak values (around 0, 0.1, 0.3, and 0.45 s). This continued for about 3 weeks until around 27 October, the time when the concentrated distribution of ϕ_{pol} at around 30° also ended at this station. At EOBS 2 and LOBS 7, δt remains near 0 s while ϕ_{pol} is stable. There are two cases in which δt is near zero: (a) the medium is isotropic and no splitting takes place, or (b) the initial polarization of the S-wave coincides with either the fast

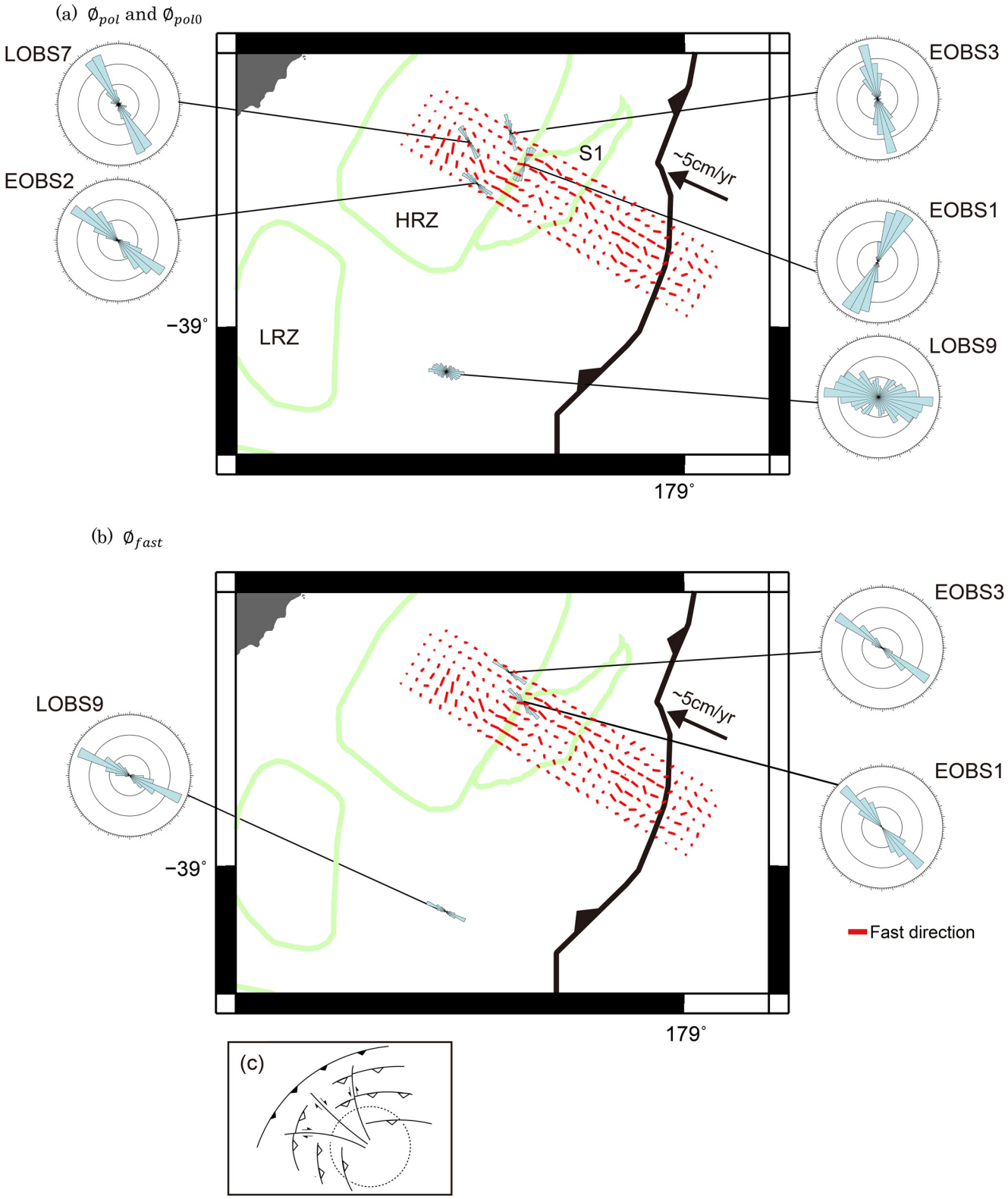
(a) $\emptyset_{pol}$ and $\emptyset_{pol0}$
LOBS7
EOBS2
EOBS3
EOBS1
LOBS9
S1
~5cm/yr
HRZ
LRZ
−39°
179°
(b) $\emptyset_{fast}$
LOBS9
EOBS3
~5cm/yr
EOBS1
−39°
Fast direction
179°
(c)

Figure 7.

or the slow orientation of the medium (e.g., Wustefeld & Bokelmann, 2007). Therefore, using only this method, we cannot distinguish those two cases. When δt is 0 s, ϕ_{fast} has no meaning. At that time, ϕ_{fast} is affected by ϕ_{pol} and may tend to have directions rotated by $\pm 45°$ from ϕ_{pol}, and high CC is obtained when λ_2/λ_1 is low. At EOBS 4 and 5 and LOBS 3, where no consistent ϕ_{pol} directions were observed, no consistent ϕ_{fast} directions are seen during the year-long experiment.

To further inspect the delay time δt, we plotted the distributions of time lags at each station at the time when we observed stable ϕ_{fast} at EOBS 2 and 3 and LOBS 7 and 9 or when we observed a bimodal distribution of ϕ_{fast} (around 60° and 150°) at EOBS 1 (Figure 9a). For comparison, we also plotted the distribution of time lags for an interval when we did not observe stable ϕ_{fast} at EOBS 3 and LOBS 9 or when ϕ_{fast} took regular values at around 120° at EOBS 1 (Figure 9b). At EOBS 2, the largest peak at 0 s and the second largest peaks (near $\pm$ 0.1 s) are symmetrical. At EOBS 3 and LOBS 9, there is a large peak at 0 s with a second significant peak near 0.1 s. If δt equals 0 s and cycle skipping is responsible for the second peak, the largest peak should be at 0 s with secondary peaks at $-$T/2 and +T/2 symmetrically (T = predominant period of the wave). Therefore, we conclude that the observed peak in time lag near 0.1 s results from SWS and not cycle skipping. There appears to be a third large peak near $-$0.2 s at LOBS 9. When considering the wave's predominant frequency of about 5 Hz (T = 0.2 s), the absolute value of this peak is exactly T/2 (0.1 s) larger than the second largest peak. Therefore, the third peak at 0.2 s may be the result of cycle skipping. As shown in Figure 9b, at EOBS 3 and LOBS 9, we find the largest peak around 0 s when no stable ϕ_{fast} was observed. Thus, we consider this peak near 0 s to be due to polarized noise. The preferred orientation of this polarized noise may be associated with the OBS exterior, specifically its square anchor frame. Such exterior structure may produce a resonant vibration in a certain direction. Amplification of one component over the other due to topographic affects (Pischiutta et al., 2015; Spudich et al., 1996) is another possible cause. We observe noise with some trend in ϕ_{pol} (0–60°) at EOBS 3 during the year-long observation in Figures 4–6 and S3 in Supporting Information S1. (When ϕ_{pol} takes a certain direction and delay time is 0 s, ϕ_{fast} can be the direction rotated by $\pm$ 45° from ϕ_{pol}. At EOBS 3, the trend of ϕ_{pol} range over 60° and as a result ϕ_{fast} seems to be scattered.) Similarly, at LOBS 7, the largest and secondary peaks are at 0 and at near 0.1 s, but the second largest peak seems to be a minor event and it may be difficult to ascribe this peak to SWS. At EOBS 1, there is also an asymmetrical distribution of δt with the largest peak around 0.2 s. However, there are also peaks around 0 s and at a negative time lag whose absolute value is T/2 smaller than that of the largest peak (around $-$0.1 s) but also around $-$0.3 and 0.45 s. In Figure 9b, we see a peak around $-$0.3, 0 and 0.45 s through the year-long observation at EOBS 1. Therefore, we conclude that the peak around 0.2 s represents SWS in October, the peak around $-$0.1 s can be ascribed to cycle skipping and other peaks originate from noise. At EOBS1 and 3 and LOBS 9, where we observed SWS, we estimated the initial polarization, ϕ_{pol0} (Figures 5 and 8). As the δts used to compute initial polarizations include the effect of noise and cycle skipping, their values are bimodal and scattered (Figures 5 and 8). Thus, we extracted the ϕ_{pol0} that corresponds to the δt only near the value estimated as the delay time (around 0.23 s at EOBS1, 0.12 s at EOBS 3, and 0.09 s at LOBS 9) (Figures 5 and 8). The direction of ϕ_{pol0} during the continuous signals at EOBS 1 and 3 and LOBS 9 were calculated using day-long data and plotted at the respective OBS sites in Figure 7a. The directions of ϕ_{fast} during the continuous signals at these same stations were also calculated using day-long data and are also plotted at their respective OBS sites in Figure 7b.

4. Discussion

4.1. Continuous Signal With Stable Polarization Direction

At stations EOBS 1, 2, and 3, and LOBS 7 and 9, polarization and SWS analyses parameters from continuous signals remained stable for an overlapping period of approximately 2 weeks starting at the end of the 2014 SSE, when slip was tapering off. Previous studies suggested that these parameters are stable and CCs high while tremor activity occurs near the recording station (e.g., Bostock & Christensen, 2012; Imanishi et al., 2016; Ishise

Figure 7. (a) Representative ϕ_{pol} at EOBS 2 and LOBS 7 and ϕ_{pol0} at EOBS 1 and 3 and LOBS 9 during recording of continuous signal. (b) Representative ϕ_{fast} at EOBS 1 and 3 and LOBS 9 during recording of continuous signal. Rose histograms with a bin width of 10° (light blue bars) of ϕ_{pol}, ϕ_{pol0}, or ϕ_{fast} are plotted at each OBS site. Histograms are calculated using day-long data at EOBS 1 (19 October 2014), EOBS 2 (11 October 2014), EOBS 3 (16 October 2014), LOBS 7 (8 October 2014), and LOBS 9 (14 October 2014). Rose histograms in (b) are calculated when the time lag is near the value that we estimated as delay time for tremor (0.21 $\leq$ time lag[s] $\leq$ 0.25 at EOBS 1, 0.1$\leq$ time lag[s] $\leq$ 0.15 at EOBS 3 and 0.07 $\leq$ time lag[s] $\leq$ 0.11 at LOBS 9). Subducted seamounts S1, high-amplitude reflectivity zones, lens reflectivity zone and the convergence direction between the Pacific Plate and the North Island at the Hikurangi Trough are shown with light green lines and black vector. P-wave fast directions at 1 km depth below seafloor from Arai et al. (2020) are shown with red bars whose lengths are proportioned to the anisotropy magnitudes. (c) Tectonic interpretation of a conical seamount subduction (dotted line) showing the relations between the different fracture networks (from Dominguez et al., 1998).

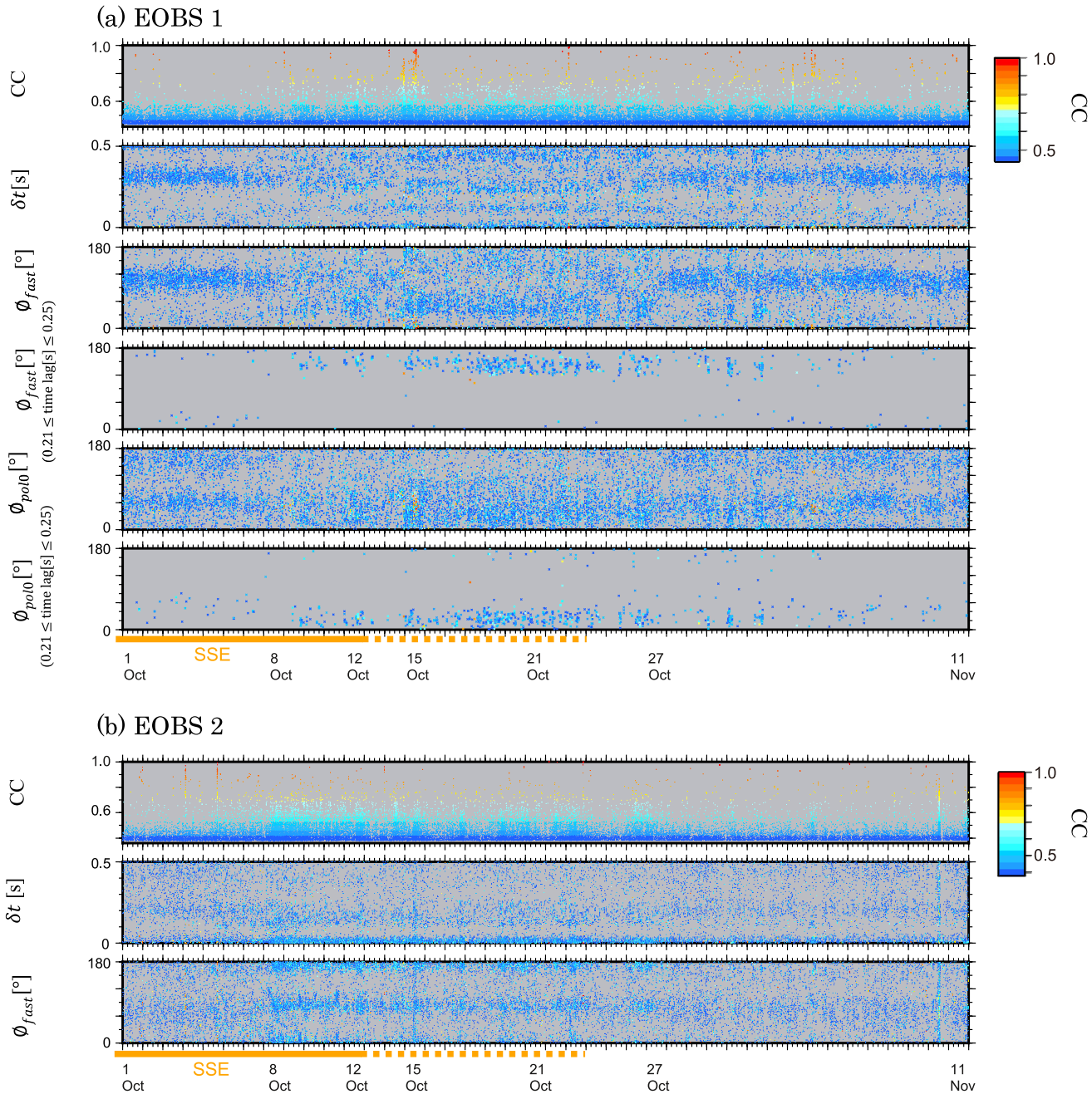

Figure 8. Times series from October 1 to November 11 of S-wave splitting parameters for EOBS 1 and 2 and LOBS 7 and 9. The panels show, in descending order, Cross-correlation coefficients (CC), δt, ϕ_{fast}, and for EOBS 1 and LOBS 9 the estimated original polarization directions, ϕ_{pol0}, is also shown. ϕ_{fast} and ϕ_{pol0} are measured clockwise from north. At LOBS 7, we sometimes observe noise which has high CC. The late September–early October 2014 Gisborne slow slip event (Wallace et al., 2016; Yohler et al., 2019) is shown by the orange bar and the dashed orange bar in the same manner as in Figure 4.

& Nishida, 2016). Consistent with these previous studies, we interpret the continuous signals exhibiting stable ϕ_{pol} and high CC in our data as tremor activity. At EOBS 1, ϕ_{pol} and SWS parameters remained stable for most of the year, but in October, during the final stages of the SSE (after the main pulse of slip had finished; Yohler et al., 2019), they changed their value for a period lasting about 2 weeks (October 15–27). We think that this change in ϕ_{pol} and SWS parameters is due to the arrival of tremor signals. Previous studies (e.g., Bostock & Christensen, 2012; Imanishi et al., 2016) have not focused on the time development of ϕ_{pol} as evidence of tremor. We expect periods of near stable polarization direction to arise from the initiation of a nearly stationary source

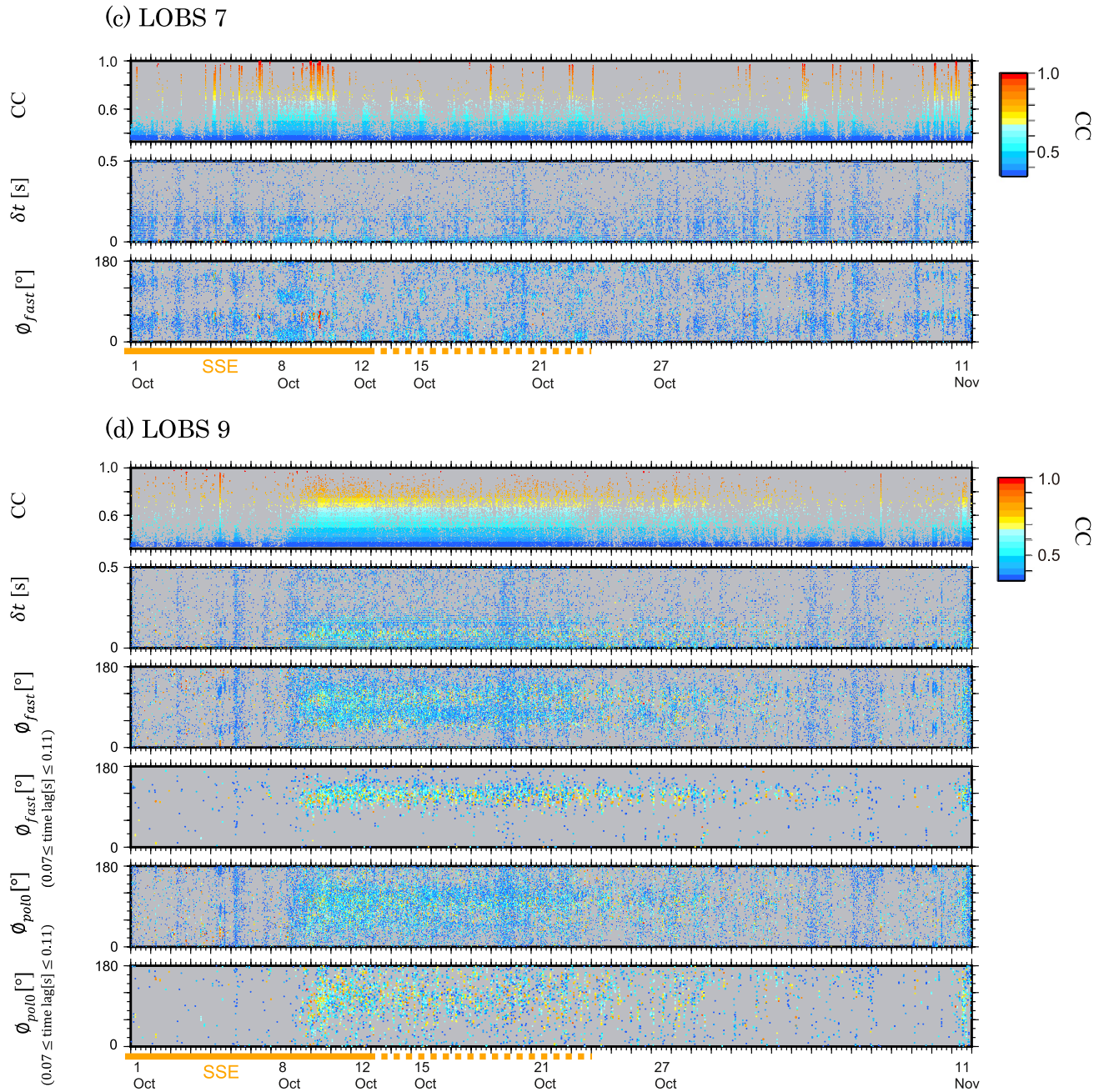

Figure 8. *Continued*

with a consistent mechanism, such as tremor. However, the year-long stable polarization direction at EOBS1 is more likely caused by a preferable orientation of noise, likely associated with the OBS exterior or topography (Pischiutta et al., 2015; Spudich et al., 1996), and the relatively short-term change in this polarization direction likely heralds the arrival of tremor signals.

To confirm that the change in parameters observed at each station is due to tremor activity, we examined horizontal seismograms for evidence of tremor during this period. First, we selected two time periods of one hour each near the beginning (4–5 p.m. on 15 October 2014) and in the middle (6–7 a.m. on 21 October 2014) of the continuous polarization period with high CC and examined waveforms and spectrogram at EOBS 3 (Figure 10). During these hour-long periods, we can observe the tremor-like waveform continuously. We also examined the waveforms from other stations during one hour periods when we observed continuous polarization with high

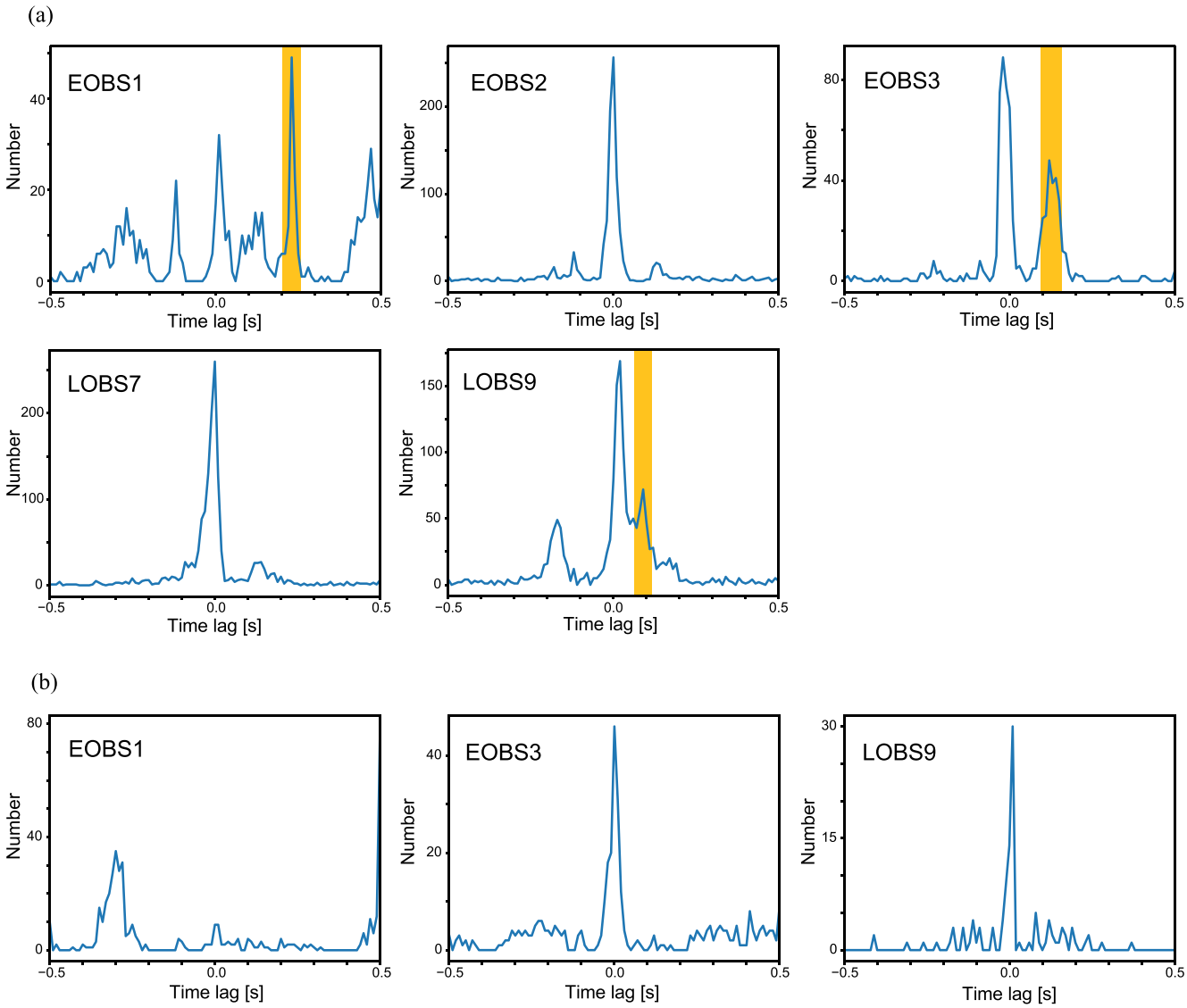

Figure 9. (a) Distribution of time lags during recording continuous signal. Each distribution is obtained from day-long data observed at EOBS 1 (19 October 2014), EOBS 2 (11 October 2014), EOBS 3 (16 October 2014), LOBS 7 (8 October 2014), and LOBS 9 (14 October 2014). At EOBS 1 and 3 and LOBS 9, where we observed S-wave splitting, the lag times which are estimated to come from signals and are used to obtain ϕ_{fast} and ϕ_{pol0} are high-lighted with orange shaded rectangles respectively. (b) Distribution of the time lags when we did not observe continuous signal. Each distribution is obtained from day-long data observed at EOBS 1 (3 September 2014), EOBS 3 (9 August 2014) and LOBS 9 (25 August 2014).

CC (Figure S4 in Supporting Information S1). The continuous tremor-like activity is also observed at these stations. Second, we examined the temporal change of amplitude of horizontal component seismograms at all OBS stations. The quantitative values of root mean square (RMS) amplitude during the continuous polarization period compared to the long time average are shown in Table S1 in Supporting Information S1. The RMS amplitude of the longer time series from July 2014 to March 2015 is shown in Figure S5 in Supporting Information S1. During the time period of a change in ϕ_{pol} at station EOBS1 and stable ϕ_{pol} and high CC at nearby station EOBS 3 (between October 15 and 27), the amplitude at these stations became larger than the long-time average (Figure 6a). At nearby stations EOBS 2 and LOBS 7, an increase in amplitude occurred synchronously with their period of stable ϕ_{pol} and high CC, between about October 8 and 27. Similarly, at the more distant station LOBS 9, amplitude increased during its period of continuous signal (October 9–21). These results suggest that while continuously polarized signals occur at one OBS, the source of tremor is near that station and the amplitude of the signal increases. Thus, at that station, the signal-to-noise ratio is high enough to obtain ϕ_{pol} of tremor, but too low to identify ϕ_{pol} at a more distant station. Considering these observations, we conclude that continuous signals

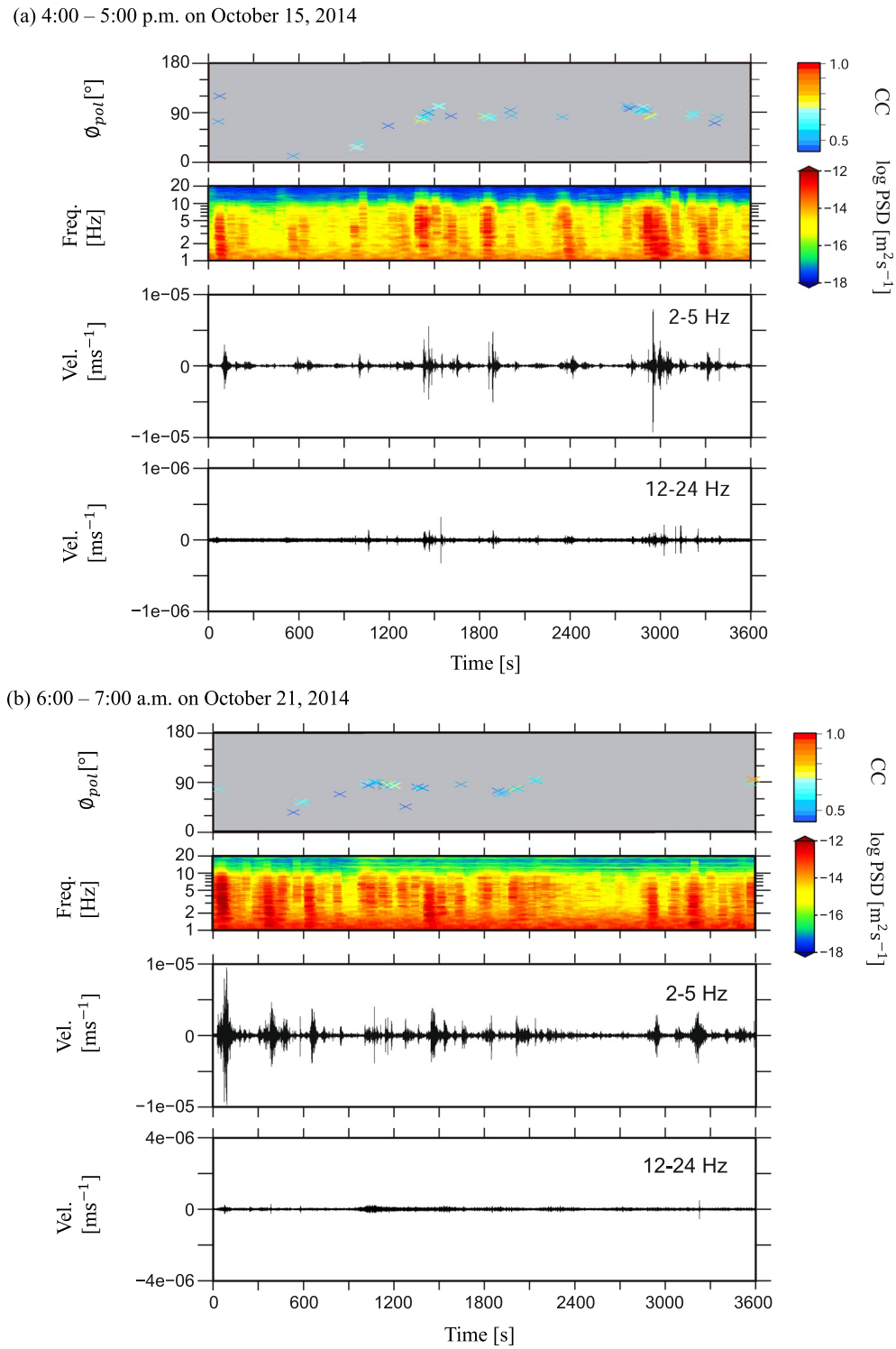

Figure 10. Seismic records of one of the horizontal components and spectrograms at the time when we recorded continuous signal at EOBS 3. The polarization directions, ϕ_{pol}, are colored according to the value of the of Cross-correlation coefficients. The panels show, in descending order, ϕ_{pol}, spectrogram, seismic coda (ms^{-1}; filtered 2–5 Hz), and coda (filtered 12–24 Hz). The power spectral density is calculated using 1-minute-long data windows of the horizontal component.

exhibiting stable ϕ_{pol} indicate tremor activity near the station that continues to occur with near stable location and mechanism.

To determine if the near continuous tremor we identify is co-located with tremor events previously identified by Todd et al. (2018), we compare ϕ_{pol} values for time periods of tremor events in the Todd et al. (2018) tremor catalog to our continuous values during the same time periods at stations near the seamount (EOBS 1, 2, and 3, and LOBS 7). Often when CC values are high, there is good agreement between ϕ_{pol} values (Figure S6 in Supporting Information S1) and tremors are located very close to the stations (Figure S7 in Supporting Information S1). We also observe ϕ_{pol} in tremor event time periods with high CC that are distributed in a different direction from that of the continuous signal; this may represent signals from a different mechanism or path. In general, when CC is low ϕ_{pols} are scattered. Detected tremors are found to be mainly distributed within a ∼10 km radius (Figure S8 in Supporting Information S1). Since, each discrete tremor source is only observed at a few closely spaced stations, we conclude that it is localized very close to the observing stations. If tremors are considered to occur near the plate interface, at ∼7 km depth, the generated signal may not propagate directly through the overriding plate, but through the oceanic crust and influence the polarization direction. However, Arai et al. (2020) find the magnitude of P-wave azimuthal anisotropy to be small (<2%) beneath the plate interface, in the vicinity of tremor observations, and heterogeneous and variable (>5%) in the overriding plate. Therefore, we consider that the observed S-wave polarization anisotropy originates in the upper crust (<∼4 km depth). In addition to that, the ray path of the S-wave may be nearly vertical in the shallow part because of its low velocity. When we consider it with the wavelength (about 200–500 m), the anisotropy we observed came from the structure whose size is about an order of 1 km just under the station. The method of this confirmation is described in Text S1 in Supporting Information S1. S-wave splitting fast orientations from local earthquakes (Zal et al., 2020) also matched remarkably well to the P-wave anisotropy observed by Arai et al. (2020), suggesting that S-wave anisotropy has a similar fast orientation to P-wave anisotropy and is also mainly shallow. Some of the tremors in the catalog of Todd et al. (2018) were not detected at any station and tremors with low CC have a wide range of ϕ_{pol}. We examined the amplitude difference between detected and undetected tremors at each station and found that events with large amplitude were generally detected. Our criteria of tremor detection include stable polarization or SWS of the tremor signals that may be generated at small patches on a fault plane. It may be difficult to detect tremors generated at small faults of a wide range of orientation, especially within a complex structure around a subducted seamount.

4.2. SWS Parameters

We did not observe SWS at EOBS 2 and LOBS 7. At these stations, ϕ_{pol} is similar to ϕ_{fast} reported by Arai et al. (2020) and Zal et al. (2020) (Figure 7). Thus, we conclude that the lack of splitting is due to the similarity of the original polarization from the tremor to the fast direction of the medium, although we cannot rule out the possibility that the medium in the vicinity of these stations is isotropic only from our result. SWS was detected at EOBS 1, EOBS 3 and LOBS 9. The fast directions, ϕ_{fast} and the delay times, δt were around 135°, 0.23 s, 125°, 0.12 s, and 115°, 0.09 s, at these stations respectively. The fast directions are within 20° and the delay times within 0.07 s of the results reported by Zal et al. (2020). One explanation for the differences in ϕ_{fast} and δt between these studies is that Zal et al. (2020) analyzed waveforms from earthquakes whose hypocenters were more distant from the stations than the tremor activity analyzed in this study. The obtained fast direction at EOBS 1 and 3 and the larger magnitude of anisotropy at EOBS 1, compared to EOBS 3, are similar to the results reported by Arai et al. (2020) (Figure 7). All ϕ_{fast} are nearly parallel to the convergence direction between the Pacific Plate and the North Island at the Hikurangi Trough (Wallace et al., 2004). This is reasonable since we expect ϕ_{fast} to align with the maximum horizontal stress, which is subparallel to the convergence direction in this region (Townend et al., 2012).

4.3. Tremor's Mechanism and Relationship With SSE

Considering the above results, the ϕ_{pol0} and ϕ_{pol} shown in Figure 7a are the original polarization directions of tremor at the source and reflect the focal mechanism of tremor. The original polarization directions at the station on the subducted seamount are not parallel to the convergence direction between the Pacific Plate and the North Island, but instead appear to be normal to the contour lines of the seamount (except at EOBS 1). Dominguez et al. (1998) suggested that back-thrusts and subvertical strike-slip faults develop during seamount subduction

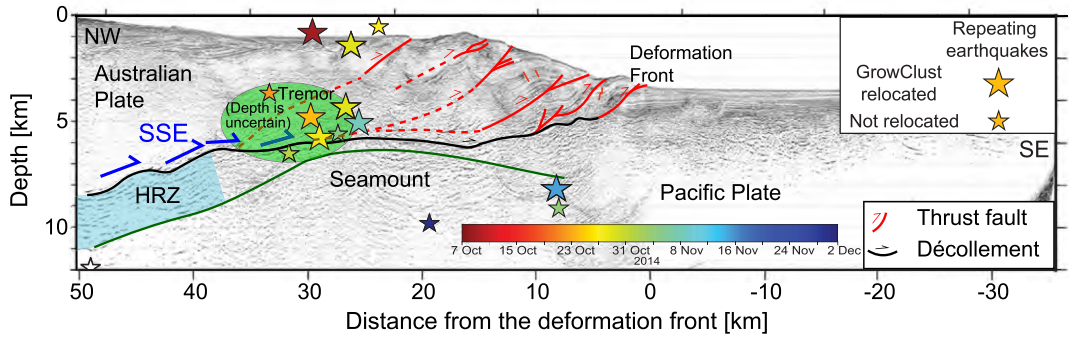

Figure 11. Interpreted prestack depth-migrated profile 05CM-04 (see location in Figure 1) (Barker et al., 2018). Active thrust faults and splay fault branching are shown in red. The plate boundary décollement and top of the subducted seamount are shown in the thick black curve and the dark green curve respectively. Repeating earthquakes identified by Shaddox and Schwartz (2019) within 10 km of 05CM-04 are shown as stars. They are colored according to time of first event within the family. Events outside of the color bar time period are white. The larger stars have been relocated with GrowClust, a relative relocation algorithm (Trugman & Shearer, 2017). The approximate region of continuous tremor activity is shaded with light green. In general, we find that tremor occurs landward of the crest of the seamount. Our results suggest that the 2014 slow slip propagates from >8 km depth in a seaward direction (indicated by blue arrows).

(Figure 7c). From the original polarization directions at EOBS 1, 2, and 3 and LOBS 7, we cannot distinguish whether tremor is located on the plate interface or in the fracture above the seamount on strike-slip faults or thrusts. However, the original polarization direction at LOBS 9 is roughly parallel to the convergence direction so it is reasonable to assume that tremor observed at that station occurred on the plate interface.

GNSS and seafloor geodetic data indicate that the main pulse of the 2014 SSE was from late September through to early/mid-October, with a tapering off period with smaller amounts of slow slip from mid to late October (Wallace et al., 2016; Yohler et al., 2019). Our results suggest that tremor activity around subducted seamount S1 and around LOBS 9 started in the period when the slow slip was tapering-off (Figure 6). Considering the tremor activity around the seamount, the location of OBS stations that detected the signals first (EOBS 2 and LOBS 7) indicates that tremor activity started at the southwest landward end of the seamount and propagated to the northeast (toward stations EOBS 1 and 3). These results are consistent with Todd et al. (2018) which located tremor by using the envelope cross correlation method. They located 0 to 12 tremors per day while we observed continuous tremor signal. Thus, our results suggest that the tremor activity occurred temporally continuously rather than as temporally isolated and sporadic individual events.

Previous studies observed concentration of tremor or VLF earthquake activity near subducting ridges or seamounts (Nishikawa et al., 2019; Toh et al., 2018; Yamashita et al., 2015; Yokota et al., 2016). Toh et al. (2018) observed a concentration of VLF earthquakes landward of the peak of the subducting-ridge with some of the events occurring along a splay fault in the eastern Nankai Trough. Shaddox and Schwartz (2019) used HOBITSS data to locate burst-type repeating earthquakes and found that most of them occurred at the landward edge of seamount S1, beginning in mid-October and continuing for about seven weeks. They suggested that during the SSE, the subducted seamount acted as an indenter into the upper plate and broke low-permeability seals in the overpressurized megathrust. This allowed fluids to migrate into the upper-plate fracture network generating the repeating earthquake activity. Zal et al. (2020) also proposed fluid migration based on a change in V_p/V_s calculated using earthquakes with the majority of ray paths traveling through the SSE patch. They reported that V_p/V_s increased in late September and then started to decrease again in late October. In addition, Todd et al. (2018) suggested that Coulomb failure stress (CFS) changes on the plate interface following the SSE are small around seamount S1. Our observations are consistent with a proposed scenario that the fluid migration into the upper plate accompanying the SSE triggered tremor activity, and further suggests that tremors were continuously generated for a duration of about 2 weeks, during the final stages of the SSE and/or just after the SSE (Figure 11). The continuous tremor activity is possibly caused by continuous fluid migration. However, we cannot conclude whether tremor is located on the plate interface or in the fracture network above the seamount.

Continuously polarized signals were also found at LOBS 9, far from the seamount. Todd et al. (2018) did not locate tremor near LOBS 9 at the time when we observe a continuously polarized signal. They were not able to

use LOBS 9 in their tremor detection and location algorithm due to timing problems. Many of the OBS used in their analyses were located near seamount S1, so tremor signals near LOBS 9 may have been masked by the large amplitude tremor activity around the seamount. Zal et al. (2020; see their Figure 5) observed a rapid change in the SWS fast direction from local earthquakes at LOBS 9 around the time of the slow slip, which could be related to noise from this tremor. Around LOBS 9, the slow slip contour is bent and large CFS changes on the plate interface are expected (Todd et al., 2018). Immediately downdip of the peak slip and seamount S1, the plate interface is also expected to experience a large increase in CFS following SSEs (Todd et al., 2018). Tremor associated with SSEs has been previously observed here (Kim et al., 2011; Todd & Schwartz, 2016). Because characteristics such as geometrical complexity or a fluid rich zone along the plate interface are not identified around LOBS 9 and it is reasonable to assume that tremor near this station occurred on the plate interface, it is possible that tremor activity here was triggered by CFS changes following the SSE.

5. Conclusion

In this study, we applied polarization and SWS analyses to continuous OBS waveforms observed in the Hikurangi subduction margin offshore New Zealand. These methods have previously only been applied to land data and usually focus on investigating anisotropy or focal mechanisms of tremor that have been previously located. Our results suggest that these methods can be used with OBS data to detect tremor, as did Ishise and Nishida (2016). We successfully detected tremor using only a few OBS. Thus, small amplitude tremor signals that are not recorded at multiple stations can still be detected. In general, the signal-to-noise ratio of OBS data is much smaller than that of data obtained by onshore seismic networks. We used the CC and the asymmetrical and unusual distribution of time lags to select the highest quality data and succeeded in applying the analysis to detect tremor. The methods in this study are likely to be applicable to many other regions.

Our results indicate continuously polarized signals starting near the end of the 2014 Mw 6.8 SSE and lasting about 2 weeks. The continuous signals indicate that tremor activity occurred near the stations with nearly the same focal mechanism. Before the 2014 SSE, shallow tremor spatially collocated with SSEs had not been detected in this region. The stations that detected the continuously polarized signals were located in a limited region. Continuous tremor activity occurred around a southwest bend within the slow slip contour and around the landward edge of the mapped subducted seamount. The tremors observed near a southwest bend in the slow slip contours were not reported in previous studies but may have been located on the plate interface and were possibly triggered by CFS changes following the SSE. Tremor activity around the subducted seamount may have occurred on the plate interface or in the upper plate fracture network developed during subduction of the seamount. This activity may be caused by fluid migration towards the end of, and following the SSE, and is consistent with seismological observations from previous studies (Shaddox & Schwartz, 2019; Warren-Smith et al., 2019; Zal et al., 2020). Our result suggests that the tremor activity occurred "continuously" for several weeks. There is a possibility that this may be caused by continuous fluid migration. Together with the results of previous studies, subducted seamounts can play an important role in influencing fluid migration and generating "continuous" tremor activity.

Data Availability Statement

Raw data from the experiment is archived at Incorporate Research Institutions for Seismology Data Management Center (IRIS-DMC) with experiment codes YH 2014-15 (seismic data) (http://ds.iris.edu/mda/YH/#YH_2014-01-01_2015-12-31).

Acknowledgments
This research was partly supported by JSPS KAKENHI Grant Number JP16H06475, ERI JURP 2013-B-09 and the Ministry of Education, Culture, Sports, Science and Technology (MEXT) of Japan, under its Earthquake and Volcano Hazards Observation and Research Program. Additional funding support came from Earthquake Research

References

Arai, R., Kodaira, S., Henrys, S., Bangs, N., Obana, K., Fujie, G., et al. (2020). Three-dimensional P wave velocity structure of the northern Hikurangi margin from the NZ3D experiment: Evidence for Fault-bound anisotropy. *Journal of Geophysical Research: Solid Earth*, *125*(12), e2020JB020433. https://doi.org/10.1029/2020JB020433

Barker, D. H. N., Henrys, S., Caratori Tontini, F., Barnes, P. M., Bassett, D., Todd, E., & Wallace, L. (2018). Geophysical constraints on the relationship between seamount subduction, slow slip, and tremor at the north Hikurangi subduction zone, New Zealand. *Geophysical Research Letters*, *45*(2312), 12804–12813. https://doi.org/10.1029/2018gl080259

Bell, R., Sutherland, R., Barker, D. H. N., Henrys, S., Bannister, S., Wallace, L., & Beavan, J. (2010). Seismic reflection character of the Hikurangi subduction interface, New Zealand, in the region of repeated Gisborne slow slip events. *Geophysical Journal International*, *180*(1), 34–48. https://doi.org/10.1111/j.1365-246x.2009.04401.x

Institute (ERI), University of Tokyo and National Science Foundation (NSF) grants: OCE-1551922 and NSF-1551683. The ocean bottom seismic data was provided by instruments from the Ocean Bottom Seismograph Instrument Pool funded by the National Science Foundation (NSF), the Earthquake Research Institute (ERI) at the University of Tokyo, and New Zealand's GeoNet project. The authors thank G.A., K.N., M.K. and K.O. for their support. The authors would also like to thank Yusuke Yamashita, Takeshi Akuhara and Yukihiro Nakatani for helpful advice and Ryuta Arai for providing the data used in Figure 7.

Bostock, M. G., & Christensen, N. I. (2012). Split from slip and schist: Crustal anisotropy beneath northern Cascadia from non-volcanic tremor. *Journal of Geophysical Research*, *117*(B8), B08303. https://doi.org/10.1029/2011JB009095

Bowman, J. R., & Ando, M. (1987). Shear-wave splitting in the upper-mantle wedge above the Tonga subduction zone. *Geophysical Journal of the Royal Astronomical Society*, *88*(1), 25–41. https://doi.org/10.1111/j.1365-246X.1987.tb01367.x

Castellazzi, C., Savage, M. K., Walsh, E., & Arnold, R. (2015). Shear wave automatic picking and splitting measurements at Ruapehu volcano, New Zealand. *Journal of Geophysical Research: Solid Earth*, *120*(5), 3363–3384. https://doi.org/10.1002/2014JB011585

Dominguez, S., Lallemand, S. E., Malavieille, J., & von Huene, R. (1998). Upper plate deformation associated with seamount subduction. *Tectonophysics*, *293*(3–4), 207–224. https://doi.org/10.1016/s0040-1951(98)00086-9

Hiramatsu, Y., Watanabe, T., & Obara, K. (2008). Deep low-frequency tremors as a proxy for slip monitoring at plate interface. *Geophysical Research Letters*, *35*(13), L13304. https://doi.org/10.1029/2008GL034342

Ide, S. (2008). A Brownian walk model for slow earthquakes. *Geophysical Research Letters*, *35*(17), L17301. https://doi.org/10.1029/2008GL034821

Imanishi, K., Uchide, T., & Takeda, N. (2016). Determination of focal mechanisms of nonvolcanic tremor using S wave polarization data corrected for the effects of anisotropy. *Geophysical Research Letters*, *43*(2), 611–619. https://doi.org/10.1002/2015GL067249

Ishise, M., & Nishida, K. (2016). *Continuous measurements of S-wave splitting parameters for monitoring of seismic anisotropy*: Poster presented at Japan Geoscience Union Meeting 2016.

Ito, Y., Obara, K., Shiomi, K., Sekine, S., & Hirose, H. (2007). Slow earthquakes coincident with episodic tremors and slow slip events. *Science (American Association for the Advancement of Science)*, *315*(5811), 503–506. https://doi.org/10.1126/science.1134454

Kim, M. J., Schwartz, S. Y., & Bannister, S. (2011). Non-volcanic tremor associated with the March 2010 Gisborne slow slip event at the Hikurangi subduction margin, New Zealand. *Geophysical Research Letters*, *38*(14), L14301. https://doi.org/10.1029/2011GL048400

Mochizuki, K., Yamada, T., Shinohara, M., Yamanaka, Y., & Kanazawa, T. (2008). Weak interplate coupling by seamounts and repeating M ~ 7 earthquakes. *Science (American Association for the Advancement of Science)*, *321*(5893), 1194–1197. https://doi.org/10.1126/science.1160250

Nakai, J. S., Sheehan, A. F., Abercrombie, R. E., & Eberhart-Phillips, D. (2021). Near trench 3D seismic attenuation offshore northern Hikurangi subduction margin, North Island, New Zealand. *Journal of Geophysical ResearchSolid Earth*, *126*(3), e2020JB020810. https://doi.org/10.1029/2020JB020810

Nishikawa, T., Matsuzawa, T., Ohta, K., Uchida, N., Nishimura, T., & Ide, S. (2019). The slow earthquake spectrum in the Japan Trench illuminated by the S-net seafloor observatories. *Science (American Association for the Advancement of Science)*, *365*(6455), 808–813. https://doi.org/10.1126/science.aax5618

Obara, K., & Kato, A. (2016). Connecting slow earthquakes to huge earthquakes. *Science (American Association for the Advancement of Science)*, *353*(6296), 253–257. https://doi.org/10.1126/science.aaf1512

Pischiutta, M., Savage, M. K., Holt, R. A., & Salvini, F. (2015). Fracture-related wavefield polarization and seismic anisotropy across the Greendale Fault. *Journal of Geophysical Research: Solid Earth*, *120*(10), 7048–7067. https://doi.org/10.1002/2014JB011560

Rogers, G., & Dragert, H. (2003). Episodic tremor and slip on the Cascadia Subduction Zone: The chatter of silent slip. *Science*, *300*(5627), 1942–1943. https://doi.org/10.1126/science.1084783

Scholz, C. H., & Small, C. (1997). The effect of seamount subduction on seismic coupling. *Geology*, *25*(6), 4872. https://doi.org/10.1130/0091-7613(1997)025<0487:teosso>2.3.co;2

Shaddox, H. R., & Schwartz, S. Y. (2019). Subducted seamount diverts shallow slow slip to the forearc of the northern Hikurangi subduction zone, New Zealand. *Geology*, *47*(5), 415–418. https://doi.org/10.1130/g45810.1

Spudich, P., Hellweg, M., & Lee, W. H. K. (1996). Directional topographic site response at Tarzana observed in aftershocks of the 1994 Northridge, California, Earthquake: Implications for mainshock motions. *Bulletin of the Seismological Society of America*, *86*, 193–208. https://doi.org/10.1785/bssa08601bs193

Todd, E. K. (2014). TAN1405 Voyage Report: Hikurangi Ocean Bottom Investigation of Tremor and Slow Slip (HOBITSS), RV Tangaroa, 10-20 May 2014. Lower Hutt, N.Z.: GNS Science. GNS Science report 2014/67.

Todd, E. K., & Schwartz, S. Y. (2016). Tectonic tremor along the northern Hikurangi Margin, New Zealand, between 2010 and 2015. *Journal of Geophysical Research: Solid Earth*, *121*(12), 8706–8719. https://doi.org/10.1002/2016jb013480

Todd, E. K., Schwartz, S. Y., Mochizuki, K., Wallace, L. M., Sheehan, A. F., Webb, S. C., et al. (2018). Earthquakes and tremor linked to seamount subduction during shallow slow slip at the Hikurangi Margin, New Zealand. *Journal of Geophysical Research: Solid Earth*, *123*(8), 6769–6783. https://doi.org/10.1029/2018jb016136

Toh, A., Obana, K., & Araki, E. (2018). Distribution of very low frequency earthquakes in the Nankai accretionary prism influenced by a subducting-ridge. *Earth and Planetary Science Letters*, *482*, 342–356. https://doi.org/10.1016/j.epsl.2017.10.062

Townend, J., Sherburn, S., Arnold, R., Boese, C., & Woods, L. (2012). Three-dimensional variations in present-day tectonic stress along the Australia–Pacific plate boundary in New Zealand. *Earth and Planetary Science Letters*, *353–354*, 47–59. https://doi.org/10.1016/j.epsl.2012.08.003

Trugman, D. T., & Shearer, P. M. (2017). GrowClust; a hierarchical clustering algorithm for relative earthquake relocation, with application to the Spanish Springs and Sheldon, Nevada, earthquake sequences. *Seismological Research Letters*, *88*(2A), 379–391. https://doi.org/10.1785/0220160188

Wallace, L. M., & Beavan, J. (2010). Diverse slow slip behavior at the Hikurangi subduction margin, New Zealand. *Journal of Geophysical Research*, *115*(B12), B12402. https://doi.org/10.1029/2010jb007717

Wallace, L. M., Beavan, J., Bannister, S., & Williams, C. (2012). Simultaneous long-term and short-term slow slip events at the Hikurangi subduction margin, New Zealand: Implications for processes that control slow slip event occurrence, duration, and migration. *Journal of Geophysical Research*, *117*(B11), B11402. https://doi.org/10.1029/2012JB009489

Wallace, L. M., Beavan, J., McCaffrey, R., & Darby, D. (2004). Subduction zone coupling and tectonic block rotations in the North Island, New Zealand. *Journal of Geophysical Research*, *109*(B12), B12406. https://doi.org/10.1029/2004JB003241

Wallace, L. M., Webb, S. C., Ito, Y., Mochizuki, K., Hino, R., Henrys, S., et al. (2016). Slow slip near the trench at the Hikurangi subduction zone, New Zealand. *Science (American Association for the Advancement of Science)*, *352*(6286), 701–704. https://doi.org/10.1126/science.aaf2349

Wang, K., & Bilek, S. L. (2011). Do subducting seamounts generate or stop large earthquakes? *Geology*, *39*(9), 819–822. https://doi.org/10.1130/G31856.1

Warren-Smith, E., Fry, B., Wallace, L., Chon, E., Henrys, S., Sheehan, A., et al. (2019). Episodic stress and fluid pressure cycling in subducting oceanic crust during slow slip. *Nature Geoscience*, *1239*(69), 475819–481822. https://doi.org/10.1038/s41561-019-0367-x

Wech, A. G., & Bartlow, N. M. (2014). Slip rate and tremor genesis in Cascadia. *Geophysical Research Letters*, *41*(2), 392–398. https://doi.org/10.1002/2013gl058607

Williams, C. A., Eberhart-Phillips, D., Bannister, S., Barker, D. H. N., Henrys, S., Reyners, M., & Sutherland, R. (2013). Revised interface geometry for the Hikurangi Subduction zone, New Zealand. *Seismological Research Letters*, *84*(6), 1066–1073. https://doi.org/10.1785/0220130035

Wustefeld, A., & Bokelmann, G. (2007). Null Detection in Shear-Wave Splitting Measurements. *Bulletin of the Seismological Society of America*, *97*(4), 1204–1211. https://doi.org/10.1785/0120060190

Yamashita, Y., Yakiwara, H., Asano, Y., Shimizu, H., Uchida, K., Hirano, S., et al. (2015). Migrating tremor off southern Kyushu as evidence for slow slip of a shallow subduction interface. *Science (American Association for the Advancement of Science)*, *348*(6235), 676–679. https://doi.org/10.1126/science.aaa4242

Yohler, R., Bartlow, N., Wallace, L. M., & Williams, C. (2019). Time-dependent behavior of a near-trench slow-slip event at the Hikurangi subduction zone. *Geochemistry, Geophysics, Geosystems*, *20*, 4292–4304. https://doi.org/10.1029/2019gc008229

Yokota, Y., Ishikawa, T., Watanabe, S., Tashiro, T., & Asada, A. (2016). Seafloor geodetic constraints on interplate coupling of the Nankai Trough megathrust zone. *Nature (London)*, *534*(7607), 374–377. https://doi.org/10.1038/nature17632

Zal, H. J., Jacobs, K., Savage, M. K., Yarce, J., Mroczek, S., Graham, K., et al. (2020). Temporal and spatial variations in seismic anisotropy and VP/VS ratios in a region of slow slip. *Earth and Planetary Science Letters*, *532*, 115970. https://doi.org/10.1016/j.epsl.2019.115970